Physical Modelling of an Aluminium Degassing Operation with Rotating Impellers—A Comparative Hydrodynamic Analysis

José Luis Camacho-Martínez[ab]; Marco A. Ramírez-Argáez[c]; Roberto Zenit-Camacho[d]; Arturo Juárez-Hernández[e]; J. D. Oscar Barceinas-Sánchez[f]; Gerardo Trápaga-Martínez[a]

[a] Materials Science and Engineering Department, CINVESTAV, Querétaro, Qro., México [b] CIATEQ A.C., El Marqués, Qro., México [c] Metallurgical Engineering Department at the School of Chemistry of the National Autonomous University of Mexico, México, D.F., México [d] Materials Research Institute of the National Autonomous University of Mexico, México, D.F., México [e] Mechanical and Electrical School at the Autonomous University of Nuevo Leon, Monterrey, Nuevo León, México [f] CICATA-IPN, Querétaro, Qro., México

PLEASE SCROLL DOWN FOR ARTICLE

Taylor & Francis
Taylor & Francis Group

Physical Modelling of an Aluminium Degassing Operation with Rotating Impellers—A Comparative Hydrodynamic Analysis

José Luis Camacho-Martínez[1,2], Marco A. Ramírez-Argáez[3], Roberto Zenit-Camacho[4],
Arturo Juárez-Hernández[5], J. D. Oscar Barceinas-Sánchez[6], and Gerardo Trápaga-Martínez[1]

[1]*Materials Science and Engineering Department, CINVESTAV, Querétaro, Qro., México*
[2]*CIATEQ A.C., El Marqués, Qro., México*
[3]*Metallurgical Engineering Department at the School of Chemistry of the National Autonomous University of Mexico, México, D.F., México*
[4]*Materials Research Institute of the National Autonomous University of Mexico, México, D.F., México*
[5]*Mechanical and Electrical School at the Autonomous University of Nuevo Leon, Monterrey, Nuevo León, México*
[6]*CICATA-IPN, Querétaro, Qro., México*

A hydrodynamic study of aluminum degassing by the rotating impeller technique was developed through experimental measurements obtained in a water physical model stirred with different impellers and air injection. The purpose of the work was to better understand degassing operation in molten aluminum through the analysis of the hydrodynamics of the system. Particle image velocimetry (PIV) was employed to measure flow patterns and turbulence characteristics of the ladle as a function of process and design variables, such as: a) impeller rotating speed (536 and 800 rpm), b) air flow rate (3 liters/min and 0 l/min), c) geometric design of the different impellers (impeller "A" made of a solid disc, impeller "B" with lateral nozzles and an impeller "C" with notches), where impellers "B" and "C" represent commercial designs.

Impellers "B" and "C" presented similar flow behavior, with radial projection and pumping effect, while impeller "A" developed different flow patterns. By increasing the angular speed and the complexity of the impeller, stirring and turbulence increased through the entire ladle, while the vortex intensity grew. Gas injection modified the liquid flow patterns reducing the magnitude of the velocity in the liquid, and significantly increasing turbulence in the ladle.

Keywords Aluminum; Degassing; Hydrogen; Mixing; Modeling; Physical; Processing; Reducing; Rotational; Turbulence.

INTRODUCTION

Quality of aluminum castings depends principally on the content of impurities in the melt, such as dissolved hydrogen, nonmetallic inclusions, and undesirable elements (iron, alkaline metals, etc.). Foundry industry has been forced to implement new technologies in order to refine aluminum more efficiently. One of the most important refining operations is the degassing that can be achieved by injecting gases through lances, porous plugs, and more recently by rotating impellers.

Rotating impellers have gained acceptance in the industry since they present an outstanding performance with the highest efficiency to remove impurities from liquid aluminum. In this method, a gas is injected into the melt through an impeller immersed in the melt which rotates at a high velocity. The impeller stirs vigorously the melt and creates a large number of small gas bubbles, which while ascending through the liquid absorb, carry, and eventually remove hydrogen and other impurities from the melt. Degassing efficiency depends on the total interfacial area

bubble-liquid (bubble sizes) and on the mass transfer rate (mixing, which depends in turn on the fluid flow patterns and turbulence of the system) [1, 2].

The most important variables in a degassing process with the rotating impeller technique are: a) ladle design and size, b) impeller design, c) location of the impeller in the ladle, d) angular speed of the impeller, e) gas flow rate and gas type, f) total injection time, and g) accessories in the ladle (dams, or any other flow modifiers). From a kinetic point of view, the following requirements are needed to efficiently remove hydrogen from an aluminum melt:

1) High interfacial area (many small bubbles);
2) Uniform distribution of bubbles in the ladle;
3) Long residence time of bubbles in the melt to reach chemical equilibrium of hydrogen;
4) Good mixing in the ladle to promote convective mass transfer of hydrogen atoms;
5) Presence of turbulence to promote mass exchange at the liquid–bubble interface [3];
6) Reduction of surface vortex to reduce air entrainment.

Physical modeling has been used extensively in metallurgical process engineering to optimize existing operations and design new processes, but more importantly they help to understand complex phenomena in the processes that are difficult to measure or visualize in metallurgical reactors.

Water physical models have been widely used in metallurgical processes involving injection of gases into molten metals for refining purposes [4]. In the case of liquid aluminum, water physical modeling has been used to study hydrogen removal by injection of gases through lances, lances with helycoidal plugs, porous plugs, diffusers, rotating impellers, rotating nozzles, and high velocity injection through special nozzles (jet nozzles) [5–16].

Most of the studies found in the literature deal with full-scale physical modeling of hydrogen removal from aluminum, and they are focused on characterizing the process in terms of bubble size, bubble distribution, and residence time of bubbles by high velocity photographic and video techniques [4, 6, 12, 17]. In other studies, mixing time was reported by measuring with an electric probe the electric conductivity of an ionic tracer injected into the water [12, 18]. Absorption and removal kinetics of gases has been studied in water models by removing oxygen, previously dissolved, from the liquid with nitrogen or argon injection [5, 8–11] and also by absorption of CO into a NaOH aqueous solution [12]. In other investigations, torque measurements were performed under different operating conditions to determine the mechanical energy supplied into the system [4, 8].

With regard to the rotary impellers, most investigations have been conducted by comparing performances of impellers with commercial designs, but the results show discrepancies. Significant differences in performances associated to the impeller design have been found in some works [10], while in others it is claimed that most of the impellers present the same performance regardless of their design, under similar operating conditions [8]. However, it has been agreed that the impeller plays a key role in the process [19].

Generally, attention has been placed in the degassing kinetics including aspects such as mixing [20] and inclusion removal [17], but both aspects being functions of the hydrodynamics of the system, it is surprising that such characterizations have not been conducted yet through rigorous research [12].

In recent years, particle image velocimetry (PIV) has been extensively used to analyze hydrodynamics in other stirred tanks systems with and without gas injection [21–28]. This technique has been described in detail and in some cases physical models were used to validate with numerical models based on fluid flow calculations [29].

In this work, the hydrodynamic study of the degassing process in an aluminum ladle equipped with a rotary impeller was carried out by measuring flow patterns and turbulence in a full scale water physical model through the PIV technique. The effects of gas flow rate, rotation speed, and impeller design on the velocity fields and turbulence in the ladle were determined in this work.

EXPERIMENTAL PROCEDURE

A full scale physical model of a pilot system was built. Temperature and pressure differences between the pilot system and the model were accounted in the scaling procedure. The gas flow rate was determined by scaling the gas injection rate in the pilot system, by considering that

TABLE 1.—Principal dimensions of the physical model and experimental conditions.

Symbol	Parameter	Dimension
D_r	Impeller diameter (mm)	A and C = 106; B = 100
H	Height of ladle (mm)	540
D	Ladle diameter (mm)	320
D_F	Shaft diameter (mm)	36
H_l	Water level in ladle (mm)	375
H_r	Height of impeller from the bottom of ladle (mm)	75
Q_g	Air flow rate (l/min)	0 and 3
	Impeller design	A, B, and C
N	Rotating speed (rpm)	536 and 800

there are density ratio differences between argon/aluminum and air/water systems, and by establishing a dynamic similarity criterion based on the modified Froude number, N'_{Fr} [9]. It was determined that the amount of air to be injected into the model is 1.08 times the volume of gas injected into molten aluminum. Table 1 shows the main dimensions of the physical model. Figure 1 shows a schematic view of the experimental setup, which uses a motor with variable speed connected to a Nylamid® shaft through a rotary joint through which gas may be injected. The gas injection system consists of several valves, a pressure regulator, and a rotameter to control pressure and air flow rate, respectively.

A cylindrical tank (representing the ladle) was made of transparent acrylic, and it was placed inside a cube of the same material to avoid distortion in the visualizations and to minimize refraction of the inner cylindrical recipient.

Figure 2 shows three geometric designs of impellers. Impeller: "A" made of a solid disc, impeller "B" with lateral nozzles, and an impeller "C" with the same design of impeller "B" but with additional notches. Impellers "B"
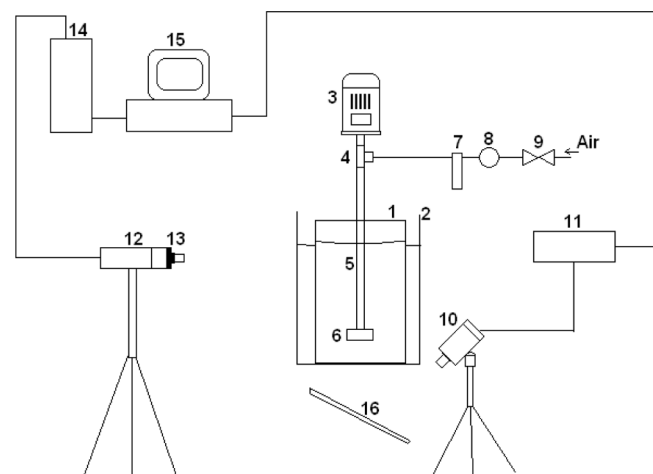

FIGURE 1.—Experimental setup: 1. Ladle, 2. External recipient, 3. Variable speed engine, 4. Rotary joint, 5. Shaft of nylamid, 6. Impeller, 7. Flowmeter, 8. Pressure regulator, 9. Valve, 10. High speed camera, 11. Sinchronizer, 12. Optical arrangement, 13. Laser generator, 14. Power source, 15. Computer, and 16. Flat mirror.
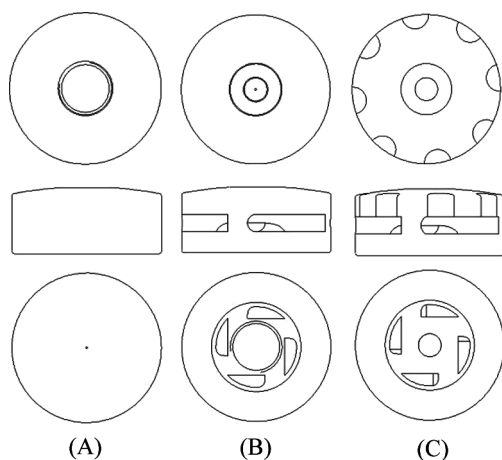
FIGURE 2.—Impellers "A," "B," and "C".

TABLE 2.—Calculated Reynolds numbers, Re, as a function of the V_{tip} and impeller diameter. Water kinematic viscosity, $\nu = 1 \times 10^{-6}\,m^2/s$.

| | D_r (mm) | | | |
| | 100 | | 106 | |
N (rpm)	Re	V_{tip} (m/s)	Re	V_{tip} (m/s)
536	89,333	2.806	100,375	2.975
800	133,333	4.189	149,813	4.440

was a LASER SOLO PIV (New Wave Research) Model SOLO III 15 Hz, synchronized to a camera KODAK MEGA PLUS Model ES 1.0 (DANTEC Systems). The fluid was water with particle tracers of polyamide of 50 μm, dyed with Rhodamine B. Acquisition and analysis conditions were: 50 pair of photographs, each pair every 500 ms, time between exposions was 1000 μs, for a total time of 25 s for every experiment. To perform the image analysis, the cross-correlation method with integration areas of 32×32 pixels was used, equivalent to a frame of 6×6 mm with an overlap of 50%. Every set of conditions was run and measured by triplicate, and these data were statistically analyzed to obtain a single velocity vector map for each plane and for each test.

Experiments were conducted according to the experimental conditions shown in Table 1. In Table 2, the values of the Reynolds number for each experiment are reported. Velocity vector maps, radial profiles of normalized velocity magnitude, V^*, and profiles of normalized turbulent kinetic energy, K_T^*, of the liquid phase were obtained on the planes of measurement indicated in Fig. 3. Additionally, pumping flow rate, Q_p, and the pump number, N_{Q_p}, were calculated for impellers "B" and "C" at 536 and 800 rpm, with and without air injection.

and "C" are reproductions of commercial designs by Foseco International Ltd. All impellers were made of Nylamid®.

Impellers were centrally located at the same height of 75 mm from the bottom of the recipient. Flow visualizations were done at 5 transversal planes located at 40, 90, 170, 255, and 360 mm from the bottom of the vessel, designated planes h1, h2, h3, h4, and h5, respectively. One longitudinal plane at the middle of the ladle was also chosen for flow patterns determinations. Figure 3 shows the model including planes where measurements were carried out.

For transversal planes, the laser plane was aligned parallel to the base of the ladle, while for the longitudinal plane it was aligned parallel to the radial coordinate of the ladle. Due to the size of the longitudinal plane, two overlapped shots were necessary to cover the whole domain, while for the transversal views only one shot was needed to cover the quarter of the system required to get the flow pattern due to the angular symmetry of the system. The apparatus
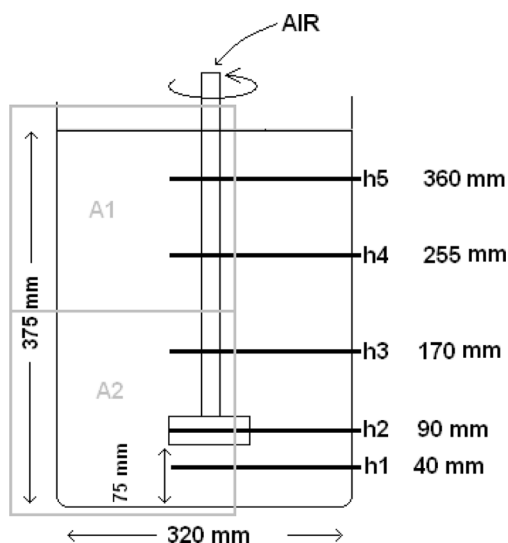
RESULTS AND DISCUSSION

Figure 4 shows photographs of the three different impellers in operation under different rotating speeds N (536 and 800 rpm), with an air flow rate, Q_g, of 3 l/min. Despite the fact that the size and distribution of bubbles were not quantitatively determined in this work, simple inspection shows that by increasing N, increases dispersion of bubbles and reduces their size; it is also observed that impellers with lateral nozzles, "B" and "C," generate smaller bubbles than the smooth impeller "A."

Flow Patterns

Figures 5–7 show velocity vector fields on the longitudinal plane obtained with different impellers, rotating at different angular speeds and without injection of air. Figure 5 presents fluid flow patterns corresponding to impeller "A" rotating at 536 and 800 rpm. Flow patterns are similar in both cases, where a radial projection of liquid from the impeller to the wall slightly directed downwards is seen at the impeller's height, which create two circulation loops, one clockwise above the impeller, and the other counter clockwise below it. In general, an increment in N promotes an increase in the velocity magnitudes in the

FIGURE 3.—Location of the longitudinal planes A1 and A2 and transversal planes h1–h5.
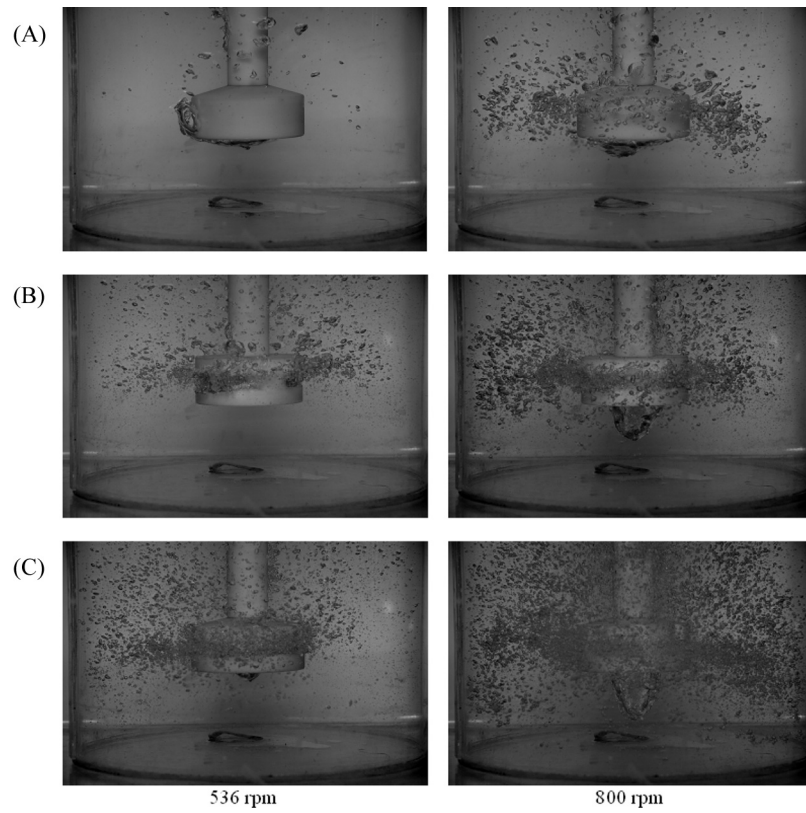
(A)

(B)

(C)

536 rpm   800 rpm

FIGURE 4.—Photographs of the physical models operating with air injection for impellers "A," "B," and "C" rotating at 536 rpm (left) and at 800 rpm (right).

(a)   (b)   (a)   (b)

FIGURE 5.—Velocity vector maps measured at the longitudinal plane for impeller "A," without gas injection rotating at (a) 536 rpm and (b) 800 rpm.

FIGURE 6.—Velocity vector maps measured at the longitudinal plane for impeller "B," without gas injection rotating at (a) 536 rpm and (b) 800 rpm.

entire ladle, but more visible in the vicinity of the impeller and close to the free surface, and at the same time the projection of liquid towards the lateral wall, the vortex and the circulation of liquid are also magnified by increasing N.

Figures 6 and 7 show velocity vector maps obtained at N of 536 and 800 rpm, corresponding to impeller "B" and "C," respectively. Similar flow patterns to those obtained with impeller "A" are observed with impellers "B" and "C" but
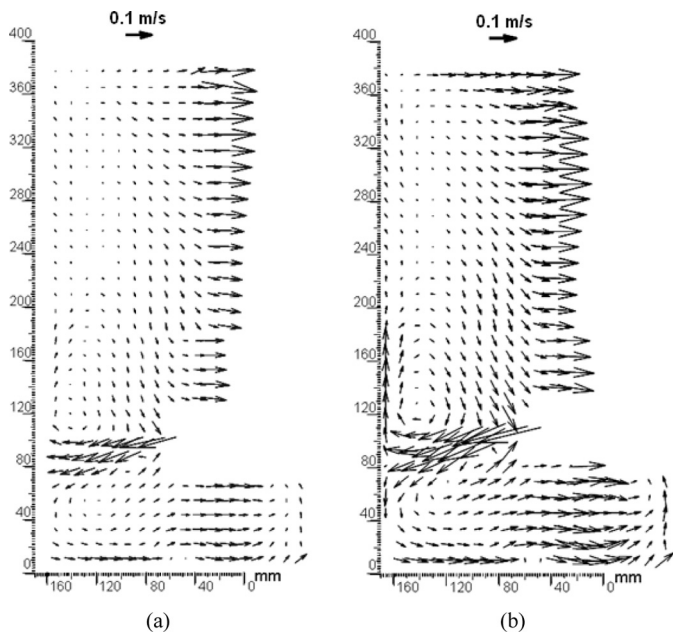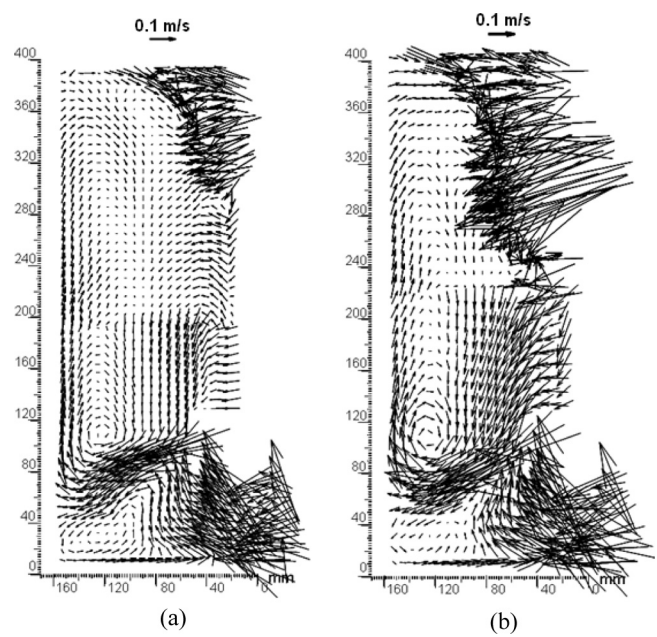
FIGURE 7.—Velocity vector maps measured at the longitudinal plane for impeller "C," without gas injection rotating at (a) 536 rpm and (b) 800 rpm.

velocity magnitudes as well as vortices are bigger. The main difference in flow patterns is the pumping effect produced by impellers "B" and "C," which is not appreciated with impeller "A." The "pumping" effect of these impellers consists on sucking fluid from the bottom of the impeller (since a low pressure is developed, because of the rotation speed creates this low pressure to counter balance the centrifugal forces), which is ejected through the lateral

FIGURE 9.—Velocity vector maps measured at the longitudinal plane for impeller "B," with gas injection rotating at (a) 536 rpm and (b) 800 rpm.

nozzles of the impeller with a high radial momentum. Impeller "C" creates the largest velocities and vortices from all impellers tested.

Figures 8–10 show the velocity vector maps obtained for the three impellers but in these cases injecting air at a rate of 3 l/min. Figure 8 shows velocity vector maps corresponding to impeller "A" with N of 536 and 800 rpm. Flow patterns are similar to those obtained without air injection (Fig. 5). However, some differences can be established: radial projection of liquid from the impeller is

FIGURE 8.—Velocity vector maps measured at the longitudinal plane for impeller "A," with gas injection rotating at (a) 536 rpm and (b) 800 rpm.
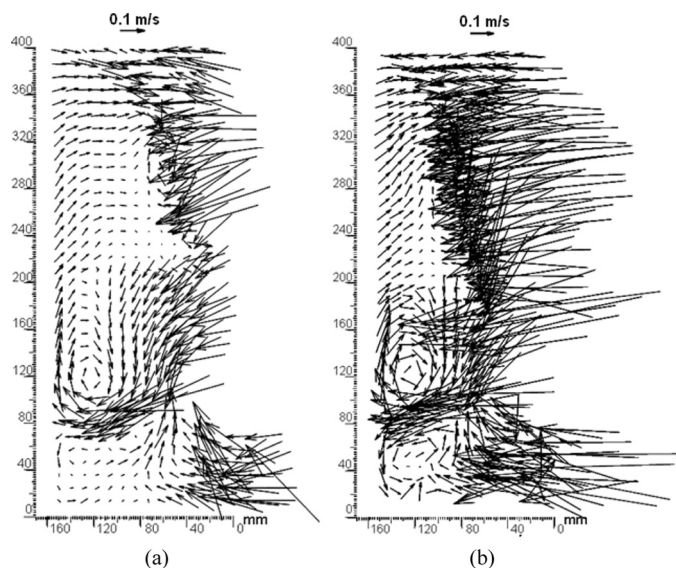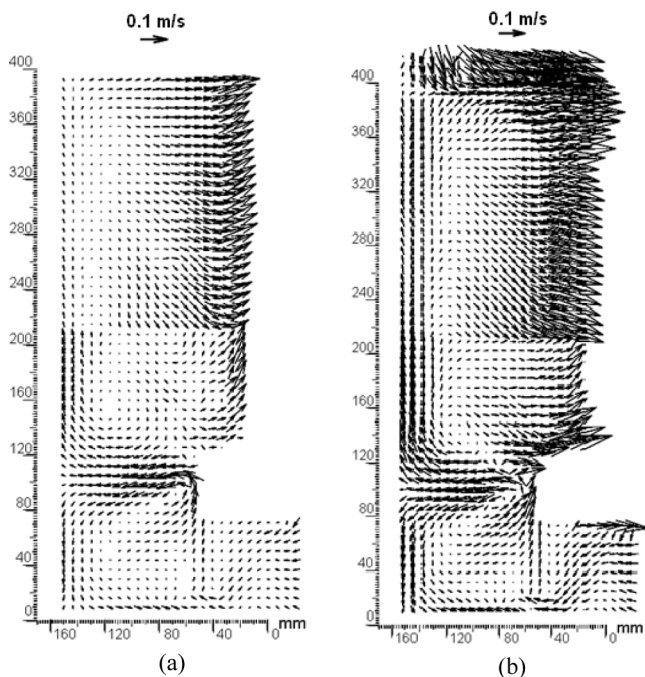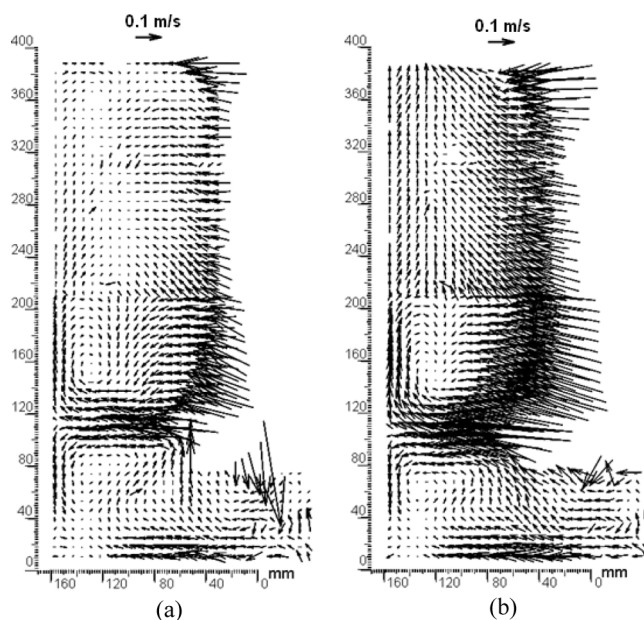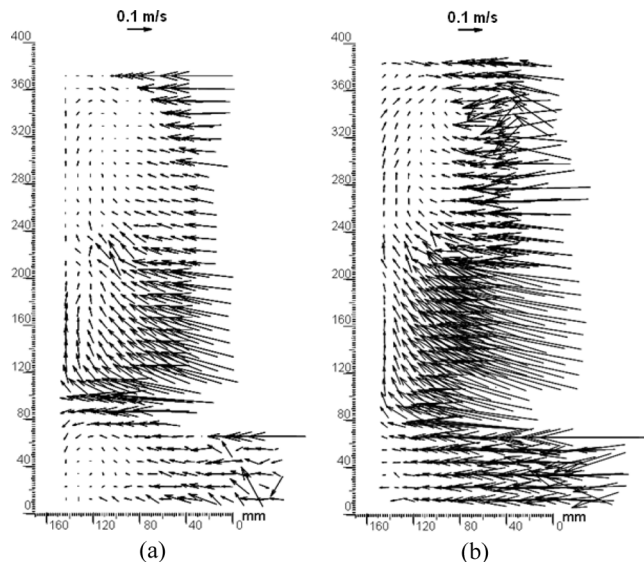
FIGURE 10.—Velocity vector maps measured at the longitudinal plane for impeller "C," with gas injection rotating at (a) 536 rpm and (b) 800 rpm.

more horizontal, and velocities are larger close to the shaft when air is injected.

Figures 9 and 10 show velocity vector maps measured at 536 and 800 rpm for impellers "B" and "C," respectively, injecting 3 l/min of air. Some differences can be readily identified when comparing flow patterns with and without air injection for impellers "B" and "C"; horizontal liquid projection, weaker circulations, smaller vortices, and pumping effect reduction when air is injected. Additionally, gas bubbles emerging from the nozzles of the impeller affect the momentum exchange (friction) between the impeller and the liquid reducing the angular motion of the liquid.

Figure 11 shows velocity vector maps measured at transversal planes h1, h2, and h4, using impeller "A" rotating at 536 rpm with and without air injection. Trends of flow patterns measured result similar in all cases regardless of the plane and the gas flow rate injected, where the angular component of the velocity dominates the flow field because the angular momentum given to the liquid by the impeller

FIGURE 11.—Velocity vector maps measured at transversal planes for impeller "A" rotating at 536 rpm; (a), (b), and (c) without air injection at planes h1, h2, and h4, respectively; (d), (e), and (f) with gas injection (3 l/min) at the same planes h1, h2, and h4. The reference vector in all cases is 0.1 m/s.

governs the fluid dynamics in the ladle. Flow perturbations observed in Fig. 11(f) are due to instabilities associated to the presence of a vortex formed at the free surface where these vectors were measured.

Radial Velocity Profiles

Maps of velocity vectors previously presented (Figs. 5–11) give a qualitative idea of the flow patterns developed in the ladle under different operating conditions. In order to obtain a more detailed analysis on the effect of the process variables on the hydrodynamics, Figs. 12–15 show radial profiles of normalized velocity of the liquid at different heights corresponding to the planes h1, h2, h3, h4, and h5. These plots give a quantitative effect of every process parameter on the hydrodynamics of the ladle.

The normalized velocity (dimensionless), V^*, was obtained by dividing the magnitude of the velocity vector, V_R, over the angular velocity of the impeller at its external radius, V_{tip}. The radial distance was also normalized by dividing the radial position over the ladle radius, R. Values of V_{tip} are shown in Table 2.

$$V^* = \frac{V_R}{V_{tip}} \tag{1}$$

$$V_{tip} = \pi D_r N \tag{2}$$

V_R, the magnitude of the velocity, was obtained as the resultant of all velocity components V_θ, V_r, and V_z

$$V_R = \sqrt{V_\theta^2 + V_r^2 + V_z^2} \tag{3}$$

Angular and radial components of the velocity were obtained through the measurements at the transversal planes, but since measurements were originally processed in cartesian coordinates, a change in the coordinate system was applied together to a statistical procedure to obtain averaged values of V_r and V_θ velocity components. The axial component, V_z, was determined from measurements in the longitudinal plane.

Figure 12(a) presents radial velocity profiles obtained with impeller "B" rotating at 536 and 800 rpm without air injection. Measurements at the five transversal planes (h1, h2, h3, h4, and h5) are included in the figure. A magnification of the rectangle of Fig. 12(a) is provided in Fig. 12(b) to separate the lines from each other to facilitate the view of the profiles. Since the impeller interferes with the flow visualizations, only measurements at the plane h1 (height below the impeller) show a complete radial profile of velocities, while the rest of profiles start at a radius of 60 mm ($r/R = 0.375$), corresponding to the radius of the impeller. The normalized radial velocity profiles are practically overlapped at 536 and 800 rpm, which mean that an increment in the angular velocity of the impeller gives a proportional increment in the velocity of the fluid.

Figure 13(a) presents radial velocity profiles with impeller "C" rotating at 536 and 800 rpm without air injection measured at planes h1, h2, h3, h4, and h5. Figure 13(b) is a zoom made from the rectangle in Fig. 13(a) to give
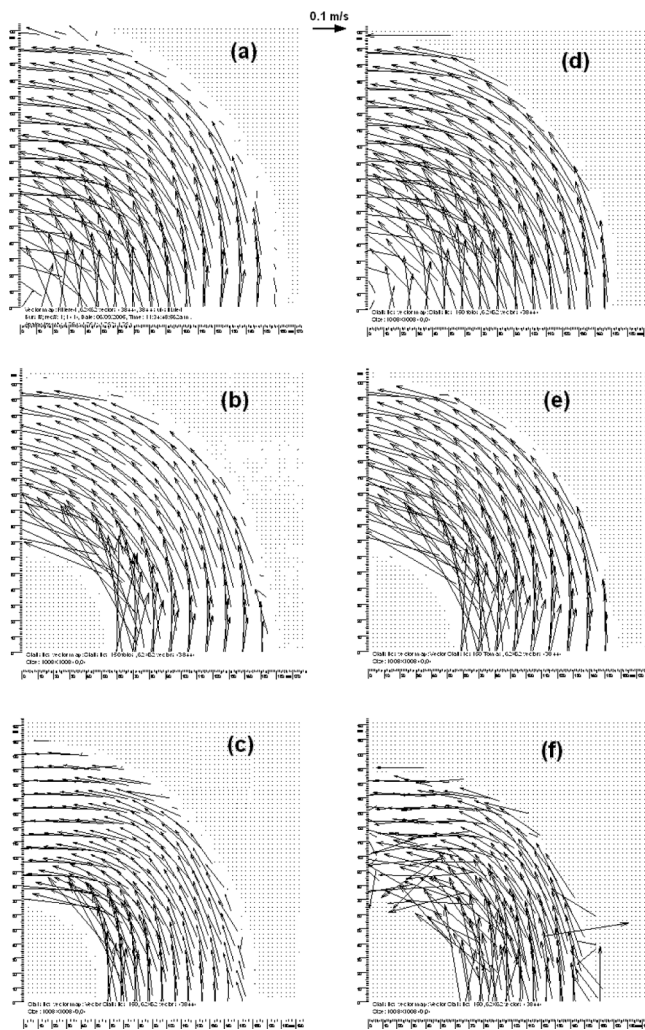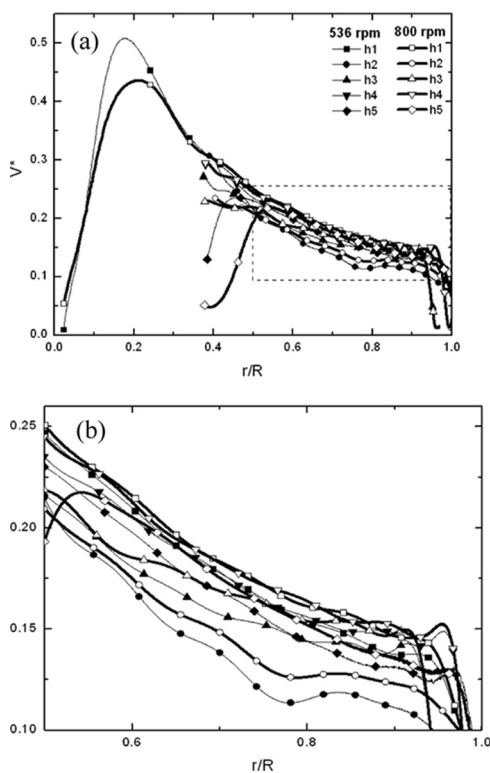
FIGURE 12.—(a) Radial profiles of V^* at transversal planes (h1, h2, h3, h4, and h5). Conditions: Impeller "B," no air injection, N of 536 and 800 rpm. (b) Magnification of rectangle in Fig. 12(a).
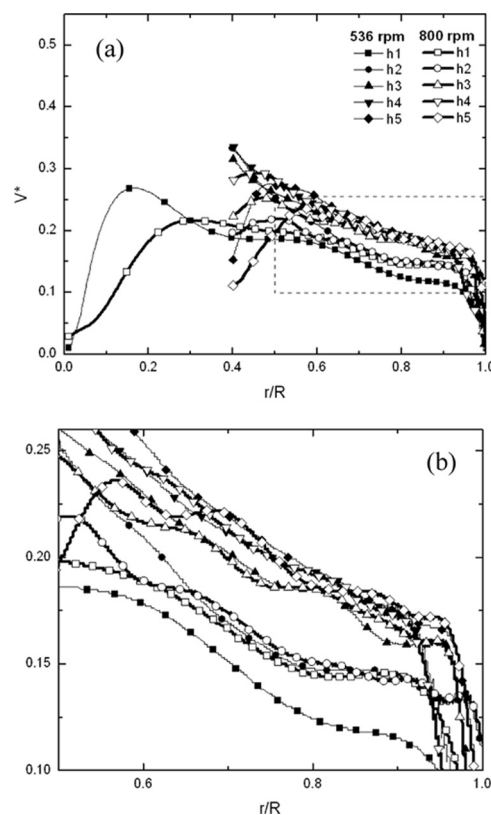

FIGURE 13.—(a) Radial profiles of V^* at transversal planes (h1, h2, and h5). Conditions: Impeller "C," no air injection, N of 536 and 800 rpm. (b) Magnification of rectangle in Fig. 13(a).

a better resolution of the lines. In the case of impeller "C" profiles do not overlap as in the case of impeller "B" but velocities depend rather on the plane of measurement. Comparing velocity profiles obtained from impeller "B" and "C," it is clear that trends are similar but impeller "C" gives in general larger magnitudes of velocity than impeller "B," which means that impeller "C" agitates better than impeller "B."

All velocity radial profiles show high values close to the center where the impeller or the shaft transfer momentum to the liquid, but as the radius increases, velocities decrease until zero at the ladle wall due to the nonslip condition.

Additionally, in these plots (Fig. 12) the maximum velocity is located at $r/R = 0.375$ (60 mm, which corresponds to the impeller radius) at the planes h2, h3, and h4, while at a plane h1, below the impeller, the maximum is at $r/R = 0.2$ (32 mm) and at the upper plane h5 (close to the free surface), the maximum velocity location varies from $r/R = 0.44$ to 0.5 (70 to 80 mm), since this maximum is located at the vortex location. Then, as N increases, the vortex also increases and the radial location of the maximum at plane h5 increases.

Figure 14 presents normalized velocity profiles at planes h1, h2, h4, and h5 obtained with impeller "B" rotating at 536 rpm, where the effect of air injection on the liquid velocity can be observed. By injecting air, liquid velocities decrease significantly regardless the axial or radial position. Additionally, the radial profiles are flatter, and there is no clear maximum in the velocity profile. This generalized

decrement in velocity with air injection may be explained due to a decrement in the angular momentum (friction) given by the impeller to the liquid, since the gas flowing out the impeller acts as a physical barrier partially destroying
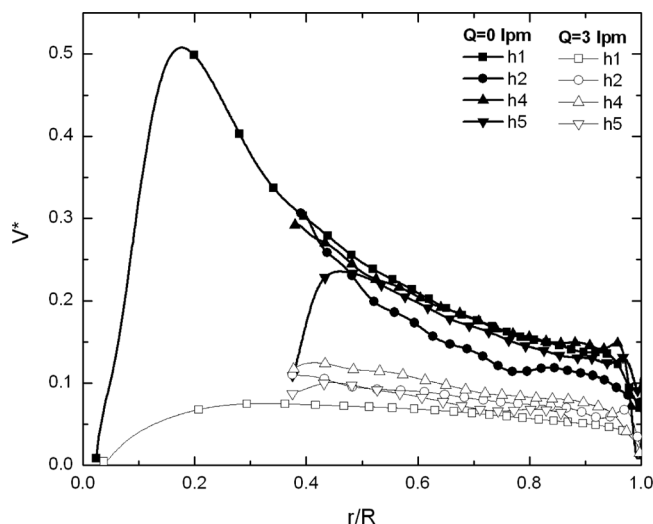

FIGURE 14.—Effect of air injection of the radial profiles of normalized velocity at planes h1, h2, h3, h4, and h5. Conditions: Impeller "B," N of 536 rpm.

the interface formed between the impeller and the liquid, avoiding an intimate contact between the impeller and the liquid. Besides, gas bubbles ascending vertically through the melt towards the free surface transfer vertical momentum to the liquid. Analyzing velocity profiles at the plane h5, it can be seen that vortex size decreases with injection of air since the maximum vanishes.

Figure 15 presents normalized velocity profiles at plane h2 (at the level of the impeller) with an angular velocity of 536 rpm, and varying the type of impeller and the air flow rate. Without air injection the velocity profiles are similar for all the impellers: there is a maximum located at the liquid–impeller interface and, as the radius increases, velocities decrease until they reach the zero value at the wall. However, the profile for impeller "A" lies below since this impeller does not present the "pumping" effect. When air is injected, the profiles are almost the same both in trend and in magnitude and, in the cases of impellers "B" and "C," their velocities decrease, as was previously explained. Impeller "C" with notches, in the absence of gas, is the impeller that transfers more efficiently momentum to the liquid than the other two impellers.

Pumping Effect

As stated above, the design of impellers "B" and "C" create a pumping effect by sucking fluid from the bottom and ejecting it through their lateral nozzles. To quantify this
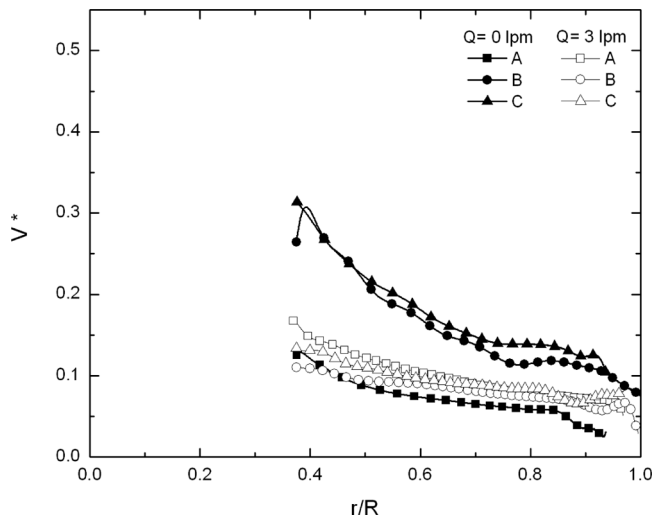

FIGURE 15.—Effect of impeller design and air injection on the radial profiles of V^* at plane h2 and N of 536 rpm.

phenomenon, the pumping flow rate was calculated, Q_p, as well as the pump number, N_{Q_p}, by using the following expressions:

$$Q_P = 2\pi \int_0^{R_r} \overline{V}_z(r) r \, dr \tag{4}$$

$$N_{Q_p} = \frac{Q_p}{ND_r^3} \tag{5}$$

Table 3 shows computed values of Q_p and N_{Q_p} for impellers "B" and "C" rotating at 536 and 800 rpm with and without injection of air. The values of these two numbers characterize efficiency of the impellers. Gas injection reduces dramatically (one order of magnitude at 536 and 800 rpm) Q_p and N_{Q_p} since the gas prevents the momentum transfer between the impeller and the liquid. Without gas injection, Q_p increases with angular velocity of the impeller "B," which results in this case in a constant N_{Q_p} number, while for impeller "C" this number is not constant, and their values are lower than those for impeller "B." In all cases tested, impeller "B" produces a higher pumping effect than impeller "C."

Turbulent Kinetic Energy Profiles

Calculations of the normalized turbulent kinetic energies, K_T^*, from experimental results were used to quantify turbulence in the ladle. By considering all fluctuating velocity components (V_x', V_y', V_z') and the operating angular velocity of the impeller (V_{tip}),

$$K_T = \frac{(V_x'^2 + V_y'^2 + V_z'^2)}{2} \tag{6}$$

$$K_T^* = \frac{(V_x'^2 + V_y'^2 + V_z'^2)}{2V_{tip}^2} \tag{7}$$

The relationships between the turbulent kinetic energy, K_T, and the turbulent intensity, IT, are

$$IT = \frac{\sqrt{2/3 K_T}}{\overline{V}} \tag{8}$$

$$IT^* = \sqrt{\frac{2}{3} K_T^*} \tag{9}$$

Figure 16 presents K_T^* vs. r/R profiles for impeller "B" without air injection at two different rotation speeds (536

TABLE 3.—Calculations of the pumped flow rate, Q_p, and pump number, N_{Q_p}, for impeller "B" and "C" at N of 536 and 800 rpm with and without gas injection.

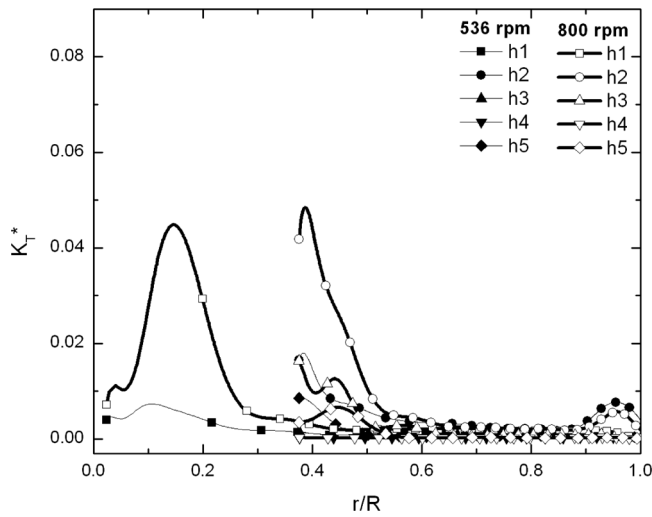|	Impeller B				Impeller C			
	$Q_g = 0$		$Q_g = 3\,l/min$		$Q_g = 0$		$Q_g = 3\,l/min$	
N (rpm)	Q_p (l/min)	N_{Q_p}	Q_p (l/min)	N_{Q_p}	Q_p (l/min)	N_{Q_p}	Q_p (l/min)	N_{Q_p}
536	60.69	0.113	5.96	0.011	50.10	0.078	−0.87	−0.001
800	89.80	0.112	8.79	0.011	53.84	0.057	−0.43	−0.0004

FIGURE 16.—Effect of N on K_T^*, at the planes h1, h2, h3, h4, and h5. Conditions: Impeller "B" and N of 536 and 800 rpm, without air injection.

the air injection effect is analyzed. Trends of K_T^* are in general similar to those presented in Fig. 16, but their magnitudes are substantially increased when air is injected (with gas injection the maximum K_T^* at plane h1 is one order of magnitude greater than the maximum obtained without injection). It is known that presence of bubbles dispersed in a liquid phase increases the turbulence intensity [23, 30]. This is due to the multiple instabilities in the motion of bubbles as they ascend through the liquid, together with the drag of these bubbles on the liquid, which give a combined effect that provides extra sources of turbulence in the liquid when gas is injected. Definitely, the great amount of small bubbles flowing through the impellers from the nozzles or from the bottom modifies dramatically the turbulence at planes h1 and h2 (close to the impeller) increasing the turbulence intensity and modifying the turbulent structure in the liquid.

Figure 18 shows the effect of the impeller design and the injection of air on the turbulence at the plane h2 and at a rotation speed of 536 rpm. Trends are similar to those observed in Figs. 16 and 17. This figure confirms that the presence of bubbles increase K_T^* though impeller "A" does not present such a big increment in turbulence. Geometric designs of impellers "B" and "C" generate more turbulence than the design of impeller "A," since the notches and lateral nozzles of the impellers "B" and "C" promote more stirring than the smooth impeller "A." Another factor increasing turbulence in impellers "B" and "C" is the pumping of fluid, since the resulting flow patterns are more complex with multiple circulations loops. Some differences can be seen in the turbulent structure produced with impeller "B" and "C." Impeller "B" produces two zones of high turbulence: one at the center of the ladle and the second close to its ladle wall. Meanwhile, impeller "C" shows a homogeneous turbulent profile, which is better distributed in the entire ladle.

Finally, Fig. 19 shows curves of K_T^* at h1 plane with air injection. Combined effects of the design of impeller with its rotating speed on the magnitude of the turbulent

and 800 rpm) plotted at the 5 transversal planes h1, h2, h3, h4, and h5 to give a complete structure of the turbulence in the ladle. Trends and order of magnitude of the radial profiles of turbulent kinetic energy (K_T^*) are similar at 536 and at 800 rpm. Zones of high turbulence are in the center of the ladle ($r/R = 0.15$) at plane h1, and close to the impeller ($r/R = 0.375$) for the rest of the planes analyzed. In the particular case of plane h2, K_T^* also increases close to the wall ($r/R = 0.95$) but at the wall ($r/R = 1.0$) decreases again. High turbulence at the center is associated to the angular motion of the impeller or the shaft, while close to the wall there is turbulence only at the level of the impeller due to the liquid projected to the wall at this level (see Figs. 4–9).

Figure 17 presents the K_T^* profiles obtained at the planes h1, h2, and h4 with impeller "B" rotating at 536 rpm, where
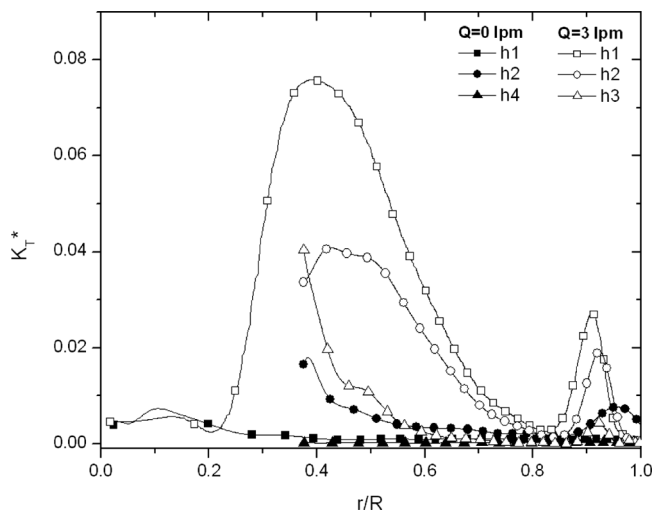

FIGURE 17.—Effect of air injection on K_T^*, at planes h1, h2, and h4. Conditions: Impeller "B," N of 536 rpm.
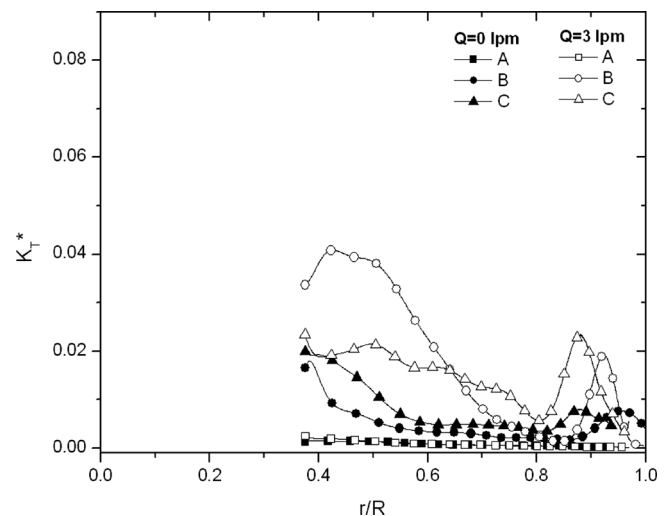

FIGURE 18.—Effect of impeller design and air injection on K_T^*, at the plane h2. Conditions: Impellers "A," "B," and "C," N of 536 rpm and air flow rate of 3 l/min.
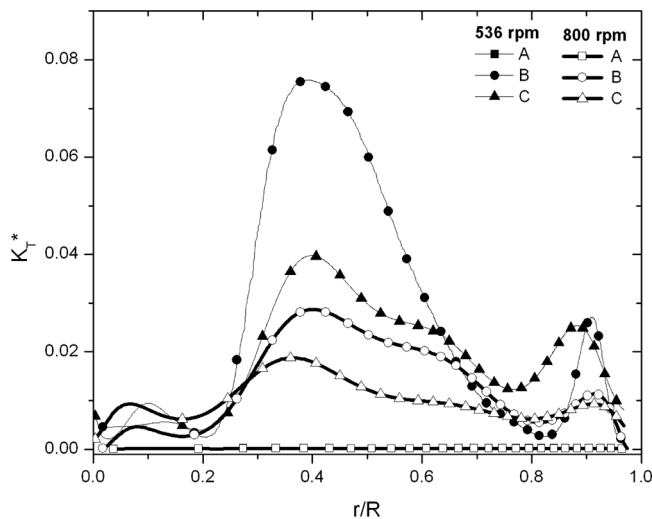
FIGURE 19.—Effect of the impeller design and N on K_T^*, at the plane h1. Impellers "A," "B," and "C" at N of 536 and 800 rpm with air injection of 3 l/min.

kinetic energy K_T^* are analyzed. It is confirmed that impeller "B" produces turbulence heterogeneously distributed being concentrated in the center of the ladle and close to its walls, while impeller "C" promotes an evenly distributed turbulence in the entire ladle.

CONCLUSIONS

Degassing kinetics in an aluminum stirred ladle equipped with a rotating impeller is governed by: a) the driving force for mass transfer (hydrogen potential difference between the liquid and the gas phases), b) the interfacial area (bubble size), and c) mixing conditions in the liquid. Mixing is in turn affected by the fluid flow patterns, strength of the convection, and degree of turbulence in the ladle. Good agitation and uniform distributed turbulence will enhance degassing kinetics. Although this work did not quantify directly the degassing kinetics, their results may be used to indirectly suggest the optimum hydrodynamics conditions to promote a better degassing performance of the degassing unit based on the characterization of fluid flow and turbulence in the liquid.

The effect of the main design and process variables such as impeller design, rotating speed, and gas flow rate on the hydrodynamics of a water physical model of aluminum degassing unit equipped with a rotating impeller, was analyzed in this investigation by measurements using PIV. The main conclusions to be drawn from this work are the following ones:

1) In the absence of air injection, velocity fields show similar trends: projection of liquid from the impeller to the ladle wall, circulations below and above the level of the impeller, and formation of vortex. Additionally, impellers "B" and "C" present a pumping effect on the fluid which does not show impeller "A," impeller "B" being the one with the highest pumping effect.

2) With air injection, fluid recirculation is reduced (or even changed), and the vortex size, the pumping effect, and the projection of liquid are also reduced.

3) Without air injection, the radial velocity profiles are similar, presenting a maximum value close to the center of the ladle and decreasing as the radius approaches the ladle wall. Air injection reduces the velocity and makes flatter the velocity profiles along radius in all planes as analyzed for impellers "B" and "C," since the presence of gas bubbles prevents momentum transport between the impeller and the liquid, while for impeller "A" there are no significant changes with or without air injection.

4) Without air injection turbulence is concentrated on the side and below the impeller, as well as next to the wall of the ladle. With air injection, turbulence increases and is better distributed through the ladle.

5) Impellers "B" and "C" produce higher turbulence than impeller "A," being heterogeneously distributed with impeller "B," while impeller "C" provides an homogeneous turbulent structure all over the ladle.

6) Mixing in the ladle is improved (and consequently degassing kinetics) with impellers "B" and "C" with high rotational speeds and gas injection, since turbulence and melt circulations are increased.

7) Impeller "C" may be considered from the hydrodynamic point of view to present the best performance of all three designs tested in this work, since promotes the strongest agitation, mixing, best bubble distribution, and a more homogeneous turbulent structure.

ACKNOWLEDGMENTS

REFERENCES

1. Warke, V.S.; Tryggvason, G.; Makhlouf, M.M. Mathematical modeling and computer simulation of molten metal cleansing by the rotating impeller degasser Part I. Fluid flow. J. Mater. Sci. Technol. **2005**, *168*, 112–118.

2. Warke, V.S.; Shankar, S.; Makhlouf, M.M. Mathematical modeling and computer simulation of molten metal cleansing by the rotating impeller degasser Part II. Removal of hydrogen gas and solid particles. J. Mater. Sci. Technol. **2005**, *168*, 119–126.

3. Harnby, N.; Edwars, M.F.; Nienow, A.W. *Mixing in the Process Industries*; Butterwort Heinemann Press: Oxford, UK, 1985; 328 pp.

4. Zhang, L.; Taniguchi, S.; Matsumoto, K. Water model study on inclusion removal from liquid steel by bubble flotation under turbulent conditions. Ironmaking & Steelmaking **2002**, *29* (5), 326–336.

5. Nilmani, M.; Thay, P.K. Gas fluxing operation in aluminium melt refining laboratory and plant investigations. Proc. of 119th TMS Annual Meeting Anaheim, CA, USA, Feb. 18–22, 1990; Bickert, M. Ed.; Light Metals 1990, The Minerals, Metals and Materials Society, 747–754.

6. Tovio, D.O.; Mugica, G.W.; González, A.C.; Cuyás, J.C. Formation and size of bubbles in degassing system of aluminun alloys. AFS Transactions **2000**, *108*, 457–462.

7. Gittery, J.R. A two years user's experience with porous plug fluxing in modern casting facility. Proc. of the 122nd Annual Meeting, Denver, CO, USA, Feb. 21–25, 1993; Das, S.K. Ed.; Light Metals 1993, The Minerals, Metals and Materials Society, 899–905.

8. Nilmani, M.; Thay, P.K.; Simensen, C.J. A comparative study of impeller performance. Proc. of the 121st TMS Annual Meeting, San Diego, CA, USA, March 1–5, 1992, Cutshall, E.R. Ed.; Light Metals 1992, The Minerals, Metals and Materials Society, 939–945.

9. Grandfield, J.F.; Irwin, D.W.; Brumale, S.; Simensen, C.J. Mathematical and physical modelling of melt treatment processes. Proc. 119th TMS Annual Meeting, Anaheim, CA, USA, Feb. 18–22, 1990, Bickert, M. Ed.; Light Metals 1990, The Minerals, Metals and Materials Society, 737–746.

10. Boeuf, F.; Rey, M.; Wuilloud, E. Metal batch treatment optimisation of rotor running conditions. Proc. of the 122nd Annual Meeting, Denver, CO, USA, Feb. 21–25, 1993, Das, S.K. Ed.; Light Metals 1993, The Minerals, Metals and Materials Society, 927–932.

11. Hjelle, O.; Engh, T.A; Raschm, B. Removal of sodium from aluminium-magnesium alloys by purging with argon and Cl2, refining and alloying of liquid aluminium and ferro-alloys. Proc. of the International Seminar on Refining and Alloying of Liquid Aluminium and Ferro-Alloys, Trondheim, Norway, August 26–28, 1985, Engh, T.A., Lyng, S., Oye, H.A., Eds.; The Norwegian Institute of Technology, Trondheim, 1985; 345–360.

12. Díaz, M.C.; Komarov, S.V.; Sano, M. Bubble behaviour and absortion rate in gas injection through rotary lances. ISIJ Int. **1997**, *37* (1), 1–8.

13. Saha, D.; Becker, J.S.; Gluns, L. A new in-line aluminum treatment system using non-toxic gases, productivity and technology in the metallurgical industries. Proc. of the International Symposium on Productivity and Technology in the Metallurgical Industries, Cologne Germany, Sept. 17–22, 1989, Koch, M., Taylor, J.C., Eds.; The Minerals, Metals and Materials Society, 1989; 855–877.

14. Le Roy, G.; Chateau, J.M.; Walker, B.D. In plant evaluation of jet cleaner metal cleaning efficiency. Proc. of the 135th Annual Meeting, San Antonio, TX, USA, March 12–16, 2006, Galloway, T.J., Ed.; Light Metals 2006, The Minerals, Metals and Materials Society, 749–752.

15. Ohno, Y.; Hampton, D.T; Moores, A.W. The GBF rotary system for total aluminum refining. Proc. of the 122nd Annual Meeting, Denver, CO, USA, Feb. 21–25, 1993, Das, S.K., Ed.; Light Metals 1993, The Minerals, Metals and Materials Society, 915–921.

16. Mi, G.; Qi, S.; Liu, X.; Niu, J. Research on water simulation experiment of the rotating impeller degassing process, Mat. Sci. Eng. A-Struct. **2009**, *499*, (1–2), 195–199.

17. Nilmani, M. A low cost solution to gas lancing problems, aluminun cast house technology theory and practice. Proc. of the 3rd Australian Asian Pacific Course and Conference, Melbourne, Victoria, Australia, July 4–8, 1993, Nilmani, M., Ed.; The Minerals, Metals and Materials Society, 117–123.

18. Peña, A.E. Análisis de algunos aspectos en el tratamiento del aluminio a través de la caracterización y el modelamiento físico y matemático (Analysis of some aspects in the treatment of aluminum through the characterization and physical and mathematical modelling), M.C. Thesis, CINVESTAV-IPN, Unidad Querétaro, Qro., México, Oct. 2004.

19. Szekely, A.G. An alternative to chlorine fluxing of aluminum: The SNIF process. Proc. of the Second Internacional Aluminum Extrusion Technology Seminar 1977, Atlanta, GA, USA, Nov. 15–17, 1977, The Aluminum Association and The Aluminium Extruders Council, 35–41.

20. Sigworth, G.K.;. Nilmani, M. Control and measurement of hydrogen in aluminum. Proc. of the 4th International Conference on Molten Aluminum Processing, Orlando Fl, USA, Nov. 12–14, 1995, AFS (American Foundrimen's Society), 675–694.

21. Fisher, P.; Cooper, P.S.; Thistlethwaite, S.R. Dissolution mechanisms in aluminium alloy additives. Proc. of the 123rd Annual Meeting, San Francisco, CA, USA, Feb. 27–March 3, 1994, Mannweiler, U., Ed.; Light Metals 1994, The Minerals, Metals and Materials Society, 1027–1032.

22. Dong, L.; Johansen, S.T.; Engh, T.A. Flow induced by an impeller in an unbaffled tank – II numerical modelling. Chem. Eng. Sci. **1994**, *49* (20), 3511–3518.

23. Aubin, J.; Mavros, P.; Fletcher, D.F.; Bertrand, J.; Xuereb, C. Effect of axial agitator configuration (up-pumping, down-pumping, reverse rotation) on flow patterns generated in stirred vessels. Trans. ICHemE **2001**, *79* (A), 845–856.

24. Hall, J.F; Barigou, M.; Simmons, M.J.H.; Stitt, E.H. A PIV study of hydrodynamics in gas–liquid high throughput experimentation (HTE) reactors with eccentric impeller configurations. Chem. Eng. Sci. **2005**, *60*, 6403–6413.

25. Bugay, S.; Escudié, R.; Liné, A. Experimental analysis of hydrodynamics in axially agitated tank. Aiche. J. **2002**, *48* (3), 463–475.

26. Escudié, R.; Liné, A. Experimental analysis of hydrodynamics in a radially agitated tank. Aiche. **2003**, *49* (3), 585–603.

27. Escudié, R.; Liné, A. Analysis of turbulence anisotropy in mixing tanks. Chem. Eng. Sci. **2006**, *61*, 2771–2779.

28. Montante, G.; Bakker, A.; Paglianti, A.; Magelli, F. Effect of the shaft eccentricity on the hydrodynamics of unbaffled stirred tanks. Chem. Eng. Sci. **2006**, *61*, 2807–2814.

29. Song, J.L.; Chiti, F.; Bujalski, W.; Nienow, A.W.; Jolly, M.R. Study of molten aluminium cleaning process using physical modelling and CFD. Proc. of the 133rd Annual Meeting, Charlotte, NC, USA, March 14–18, 2004, Tabereaux, A.T., Ed.; Light Metals 2004, The Minerals, Metals and Materials Society, 743–748.

30. Lance, M.; Bataille, J. Turbulence in liquid phase of a uniform bubbly air–water flow. J. Fluid Mech. **1991**, *222*, 95–118.